Polymer 278 (2023) 125980

Contents lists available at ScienceDirect

Polymer

journal homepage: www.elsevier.com/locate/polymer

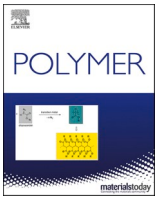

Cellulose nanocrystal-assisted processing of nanocomposite filaments for fused filament fabrication

Mia Carrola [a], Emile Motta de Castro [b], Ali Tabei [c], Amir Asadi [a,b,d,*]

[a] Department of Materials Science and Engineering, Texas A&M University, College Station, TX, 77843-3367, USA
[b] J. Mike Walker '66 Department of Mechanical Engineering, Texas A&M University, College Station, TX, 77843, USA
[c] School of Mechanical, Industrial and Manufacturing Engineering, Oregon State University, Corvallis, OR, 97331, USA
[d] Manufacturing and Mechanical Engineering Technology-Department of Engineering Technology and Industrial Distribution, Texas A&M University, College Station, TX, 77843-3367, USA

ARTICLE INFO

Keywords:
Polymer-matrix composites (PMCs)
Nano-structures
Extrusion
Anisotropy

ABSTRACT

This study introduces a scalable processing technique where cellulose nanocrystals (CNCs) are used to integrate pristine multi-walled carbon nanotubes (CNTs) into acrylonitrile butadiene styrene (ABS) polymer without functionalization, solvents, or surfactants. A synergy between the nanomaterials and printed road angle was discovered, with angle ply orientation optimizing mechanical properties and longitudinal orientation improving thermal conductivity. Mechanical properties improved up to 81% in tensile strength and 95% in elastic modulus, while a 102% increase in interlaminar strength was exhibited. The thermal conductivity trend showed an anisotropy between radial and axial directions, where one could be increased while the other was diminished, with as much as 807% increase in the transverse sample. By optimizing print orientation and nanoparticle content, tailored material properties are achievable.

1. Introduction

Additive manufacturing (AM) has revolutionized the face of manufacturing and creation through its layer-by-layer processing and this ability for production of highly custom pieces. These technologies, colloquially known as 3D printing, have opened doors in the medical field-with patient personalized implants becoming more accessible [1], in the construction industry-with the ability to print structures for housing at a rapid pace [2], and in engineering fields-for small scale prototypes and functional parts that are affordable in price. Perhaps the most accessible AM method for polymeric materials is known as Fused Filament Fabrication (FFF) 3D printing, a process that typically utilizes mainly thermoplastic filament feedstock which are extruded through a nozzle to create parts [3]. When comparing FFF to traditional manufacturing methods of polymer parts, such as injection molding, it is notably more versatile and lends itself well to parts with complex geometries and cost-effective customization of functional parts [4]. Commodity polymers such as poly (lactic acid) (PLA) and acrylonitrile butadiene styrene (ABS) are commonly utilized as feedstock for FFF due to their wide availability as well as ease of extruding at relatively low temperatures (~190–250 °C).

Despite advances in the FFF printing process itself, there is a need for improvement of the feedstock materials themselves to overcome deficits in printed parts. FFF printed parts often have poor mechanical properties, lack on-demand functionality-such as thermal and electrical conductivities, and are subject to many defects, including voids and insufficient adhesion between adjacent printed layers which result in low interlaminar strength [5–8]. Poor interlaminar adhesion and diminished flexural strength often prevent parts manufactured through FFF to be utilized as an alternative to traditional manufacturing methods, despite the complex geometries and customization potential that the process offers. Therefore, there is a need to improve the quality of these printed parts in order to allow for the widespread use of additive manufacturing in industries where traditional manufacturing techniques are not sufficient or economically practical [8]. To solve this query, many researchers have turned to improving the materials utilized for FFF printing. Several have investigated using nanomaterials as a method of adding both reinforcement and functionality in the ABS matrix of FFF filaments while maintaining the accessibility of the polymer matrix material [9–13].

Nanomaterials can possess characteristics of enhanced optical, thermal, and/or mechanical properties, all of which can be imparted on

* Corresponding author. Department of Materials Science and Engineering, Texas A&M University, College Station, TX, 77843-3367, USA.
E-mail address: amir.asadi@tamu.edu (A. Asadi).

https://doi.org/10.1016/j.polymer.2023.125980
Received 4 January 2023; Received in revised form 12 April 2023; Accepted 21 April 2023
Available online 27 April 2023

the matrix material that they are incorporated in, which makes them an attractive option for adding functionality to the composite. Previous research efforts that use nanomaterials [14–18], specifically the high strength and thermally/electrically conductive carbon nanotubes (CNTs), are lab scale and costly [19–22], often requiring multiple steps in synthesis and preparations. Though their impressive tensile strength and functional properties are highly desirable for many applications, CNTs are notoriously difficult to disperse in solution or polymer matrices, and often form agglomerates that prevent exploiting their superior properties in full. As it stands, the primary method used to integrate CNTs into the ABS matrix for FFF feedstock is known as melt compounding [17,23–26]. Melt compounding involves heating the matrix material above its melting point and adding the desired concentration of pristine or functionalized CNTs to the ABS, typically in a single or twin-screw device [27–30]. With the melt compounding method, pristine CNTs can be utilized, but often result in agglomeration throughout the nanocomposite, which can lower the effectiveness of the nanoparticles as a reinforcing material [9]. A popular alternative to using pristine CNTs and risking undesired agglomerates is functionalization of the CNTs [31]. Functionalized CNTs are carbon nanotubes that utilize an acid treatment to create functional groups on the ends of the nanotubes themselves, effectively preventing agglomeration in solution [32,33]. The use of functionalization is effective in preventing the nanotubes from agglomerating; however, it does cause damage to the material, and the results from the acid used subsequently lowers the mechanical and functional properties of the CNTs, when compared to pristine CNTs [34]. While melt compounding and CNT functionalization are effective in combining the CNTs with the ABS, they leave room for improvement and other methods to be explored that are scalable and cost effective.

One of the methods used for dispersing pristine CNTs without functionalization is by means of bonding with cellulose based nanoparticles, specifically nanocrystals (CNCs). Cellulose-a naturally occurring polymer that is harvested from sources such as wood pulp, various algae, bacteria, and plant material-is a popular material in industrial and medical fields [35,36]. Cellulose, in fact, is the most abundant renewable polymer available today, with an annual production estimated to exceed 7.5×10^{10} tons [37]. CNCs are isolated from the cellulose using mechanical and/or chemical methods, such as acid hydrolysis treatments, to create a nanoparticle which is stable in water and chemically inactive with attractive binding properties [38]. Several studies have even integrated CNCs with other materials, such as polyacrylonitrile (PAN), for improved mechanical and material performance, including in the carbon fiber composite, structural battery, and AM space [39–44]. It has been shown in traditional carbon fiber (CF) reinforced epoxy composites to increase the interfacial properties, which has been one of the primary reasons that the material has been investigated in other manufacturing operations [45]. As a result, CNCs have been introduced to various AM feedstock materials with the intention to impart higher strength and functionalities such as self-healing [46–48].

CNCs binding properties allow for the creation of well-dispersed colloidal suspensions that demonstrate liquid crystalline alignment. This attribute can be utilized to disperse other nanoparticles within a solvent, so long as the CNCs are able to bond to the nanoparticles [49]. CNCs attach to CNTs using both chemical and physical bonds and disperse the bonded nanoparticles evenly in an aqueous solution eliminating agglomerations that are typically found when using CNTs [43,50–52]. This technique is used in the place of functionalizing CNT, where the nanotubes often sustain damage due to the acid used in the functionalization process and allows for their properties to fully remain intact. Though both CNT and CNC have been utilized individually in creating nanocomposite filaments for FFF printing, they have yet to be hybridized for use together to produce a synergistic effect in any AM study. This work introduces a processing technique, in which cellulose nanocrystals (CNCs) are used as both assisting in CNT dispersion and reinforcing nanomaterials in processing. The CNCs, while serving its primary purpose of aiding in CNT dispersion, will also assist in the secondary role of adding strength in the out-of-plane direction of 3D printed parts in which increased interlaminar adhesion is expected [41].

To accommodate this gap in filament manufacturing methodology and address the need for improvement of structural and multifunctional properties in 3D printed parts, the synergistic relationship between CNC bonded CNTs must be explored in further depth as it relates to FFF feedstock and resulting printed parts. In this study, a novel manufacturing method is introduced that coats as-received acrylonitrile butadiene styrene (ABS) pellets with CNC-bonded pristine CNTs (CNT-CNC) by immersing in aqueous suspension before extrusion into 3D printing filaments. This facile processing method offers a scalable technique to create nanocomposite filaments free from agglomerates without the need for harsh solvents. The resultant CNT-CNC nanocomposite FFF filaments are used to create various characterization samples, including tensile and flexural samples as well as thermal conductivity test specimens. Additionally, the influence of the printed road angle (angle ply, longitudinal, transverse) used was evaluated in each characterization test. Increases in tensile strength and interlaminar shear strength were observed in the angle ply samples, and a unique relationship between the directionality of the thermal conductivity in these anisotropic samples was uncovered which confirms the influence of the CNT-CNC within the ABS matrix.

2. Materials & methods

2.1. Materials & equipment

Multiwalled carbon nanotubes (CNTs) [NC7000] with an average diameter of 9.5 nm, length of 1.5 μm, density of 2 g/cm^3, and number of walls being 10 were supplied by Nanocyl, Belgium. CelluForce (Quebec, Canada) manufactures the CNCs used in this study. The CNCs have an average diameter of 7.5 nm, length of 50–150 nm, surface area of 550 nm^2/g. The natural-colored acrylonitrile butadiene styrene (ABS) pellets were supplied by 3DXTECH (Michigan, USA). The filament extruder that was used in the fabrication process was the Filabot EX2 Desktop Extruder (Vermont, USA). The 3D printer used to create the various sample specimens for tensile and flexural tests is the LulzBot TAZ 6 3D Printer by Aleph Object Inc. (Colorado, USA). The printer has a maximum build volume of 280 mm × 280 mm × 250 mm and operates at temperatures of 290 °C.

2.2. Creating CNT-CNC coated ABS pellets

A suspension of CNT-CNC is created by measuring each corresponding nanomaterial with the desired concentration to ABS. The coating process is illustrated below in Fig. 1. In this study, four nanocomposite concentrations were used: 0.2, 0.5, 1, and 2 wt% CNT–CNC–ABS in addition to neat ABS as a control. These concentrations were selected based on a previous study using a similar coating method used for coating carbon fiber (CF) with CNT-CNC for use as reinforcements in carbon-fiber-reinforced-polymer (CFRP) composites, as these were the concentrations that were most stable without agglomerations present [51]. The mass ratio of CNTs to CNCs was kept to 1:1 in all samples according to this previous study, which is consistent with the ratio which provides the highest z-potential value of 51.5 mV and smallest hydrodynamic diameter of 140 nm. For each concentration, the weight percentage of the nanoparticles was measured with respect to 50 g of ABS. The measured CNTs and CNCs were added to 500 mL of deionized (DI) water and sonicated using a probe sonication device for 90 min at 75% amplitude until there were no agglomerations present in the suspension (visual inspection). Once sonicated, the suspension was added to the measured 50 g of ABS pellets in an Erlenmeyer flask and sealed for 24 h. After 24 h elapsed, the suspension was drained from the flask, while the ABS pellets were extracted.

Following the coating process, the pellets were dried in an oven for 6

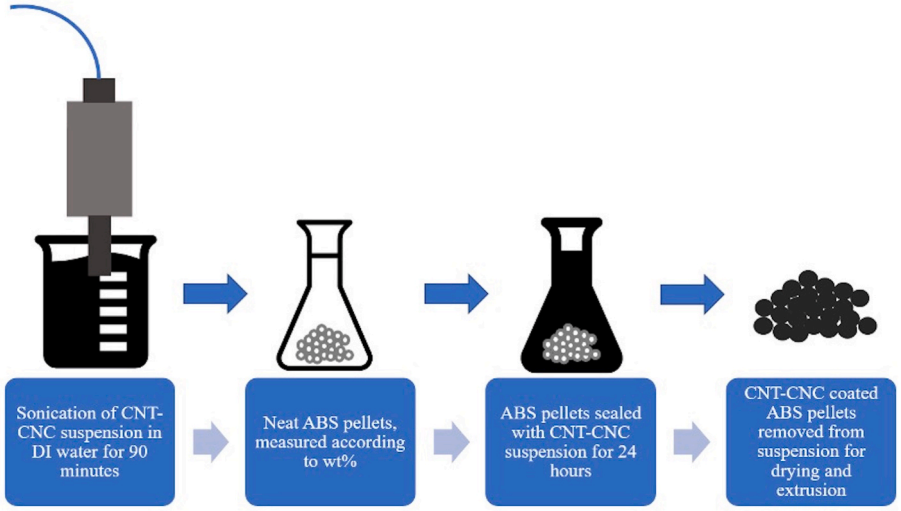

Fig. 1. Coating process for CNT-CNC suspension and ABS pellets.

h at approximately 85 °C. The drying process ensures that all excess moisture is evaporated in preparation for filament extrusion. Thermogravimetry (TGA) tests were performed to confirm that drying time was sufficient. The dried pellets were then placed in the hopper of the Filabot desktop single screw extruder and extruded at 190 °C with an average diameter of 2.85 mm. The selected extrusion parameters were based off of previous work presented by Shariatnia et al. and the standard filament size used in the Lulzbot Taz 6 printer [41]. The diameter was measured with a caliper along various points of the spool of the resulting filament to ensure uniformity and visually inspected for any imperfections such as air bubbles caused by residual moisture in the material. Each of the nanocomposite concentrations were spooled before being utilized in the Lulzbot 3D printer or stored in a filament drier at 45 °C until use.

2.3. 3D-printing samples for characterization and testing

The parameters used on the Lulzbot TAZ 6 printer are listed in Table 1 below, and are based on recommended settings for printing ABS on the TAZ 6 printer. Additional experimental optimization was utilized with neat ABS polymer in order to minimize defects such as voids. These settings maintained a consistent level of quality throughout all of the CNT-CNC nanocomposite parts. All of the samples were printed onto a Gecko-Tek EZ-Stik Hot bed liner to allow print bed adhesion to be consistent throughout the processing. Three printing orientations, i.e. longitudinal, transverse and angle ply, were used, which are detailed in Fig. 2 below.

2.4. Characterization techniques

2.4.1. Optical microscopy

Dispersion of CNT-CNC nanofillers within ABS was inspected via optical microscopy using a benchtop Olympus CH-2 optical microscope.

Table 1
3D printing parameters for additive manufacturing of CNT-CNT-ABS nanocomposites.

3D Printing Parameters	
Printing Temperature	240 °C
Print Bed Temperature	105 °C
Print Speed	40 mm/s
Retraction Speed	10 mm/s
Infill Overlap Percentage	10%
Cooling Fan	Off

Sub-50 μm thickness films were created using a manual doctor blade jig. A bead of sample polymer nanocomposite is melted on a glass slide placed on a platform heated to 240 °C. The resin bead is then scraped along the surface of the glass slide using ~50 μm stainless steel shims as a thickness guide.

2.4.2. Scanning electron microscopy

A JCM-5000 NeoScope tabletop SEM at 10 kV acceleration voltage and high vacuum mode was used to study various features of samples and filaments. For optimal image quality, filaments and printed samples were gold sputtered using a Cressington plasma sputter.

2.4.3. Thermogravimetric analysis

Thermogravimetric analysis (TGA) was performed using a TGA Q500 from TA Instruments to determine the thermal stability and the CNT content in fabricated nanocomposite pellets. The samples were heated from 20 °C to 900 °C with a 20 °C/min ramp in atmospheric air. Air instead of nitrogen was used as the stabilizing gas to decompose ABS and CNCs and mimic the thermal stability of the nanocomposite according to practical use in FFF printing. Each data point is an average of at least 3 measurements. Composite concentration was verified using the residual weight % after ABS and CNCs were in-situ decomposed with TGA leaving only CNTs. Due to the fact that the CNTs and CNCs were added at a mass ratio of 1:1, the concentration of CNCs could be estimated by the amount of remaining mass of CNTs after decomposition.

2.4.4. Tensile properties

The tensile properties of the samples were tested by using Type 1 specimens, according to ASTM D638, with a Universal United STM testing system. The system was equipped with a 10 kN load cell and tests were conducted at a displacement rate of 2 mm/min. All samples were designed with a gauge length of 50 mm, width of narrow section of 19 mm, overall width of 29 mm, an overall length of 246 mm, and a thickness of 3.175 mm. Each data point is the average of 5–7 measurements, with outlying data removed from the set.

2.4.5. Interlaminar shear strength

Short beam shear (SBS) testing according to ASTM D2344 was conducted to determine the adhesion between the printed layers by measuring the interlaminar shear strength (ILSS). The SBS testing was conducted on a Universal United STM system equipped with a 2 kN load cell with a 3-point bending setup. The displacement rate and span-to-thickness ratio were set at 2 mm/min and 4 mm/min, respectively. All samples were designed with dimensions of 40 mm × 12 mm × 7 mm.

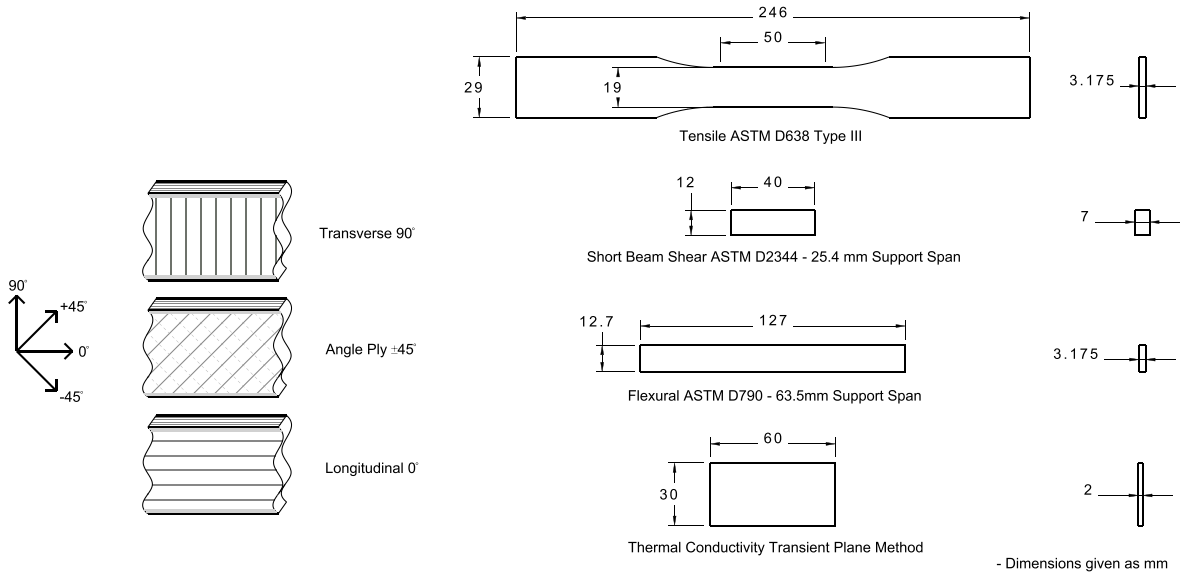

Fig. 2. Road angle orientations used for printing included a) angle ply (alternating 45° and 135° layers), b) longitudinal (0° layers), and transverse (90° layers) for all characterization samples.

The span used for all samples was 25.4 mm. Each data point is the average of at least 5 samples.

2.4.6. *Flexural strength*

The flexural strength was determined using a 3-point bending setup in a Universal United STM system equipped with a 2 kN load cell. The tests were conducted according to ASTM D790 to measure the flexural

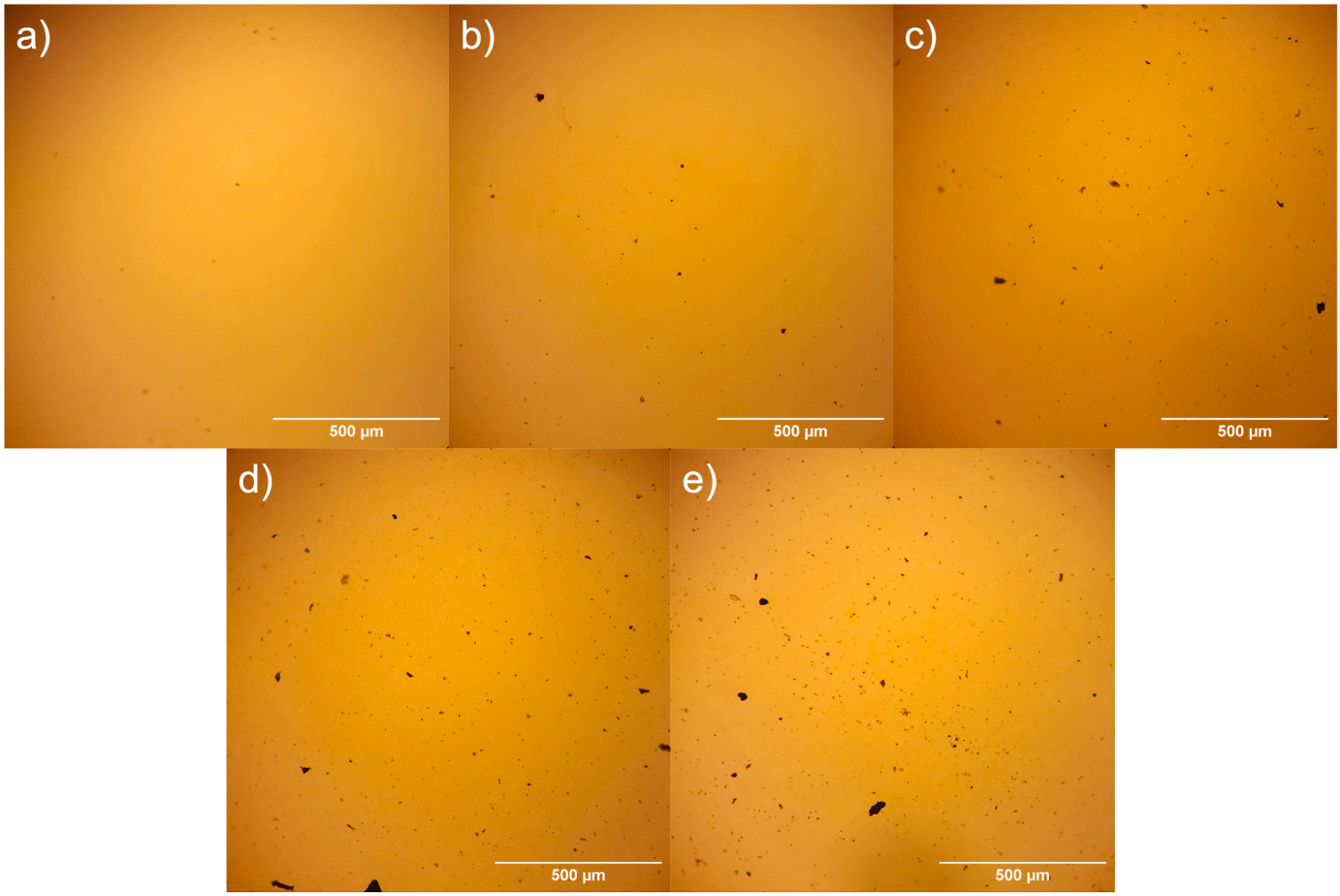

Fig. 3. Optical micrographs of ABS nanocomposite films at 10× magnification. (a)neat ABS, (b) ABS - 0.2% CNT-CNC, (c) ABS - 0.5% CNT-CNC, (d) ABS-1% CNT-CNC, (e) ABS-2wt% CNT-CNC.

strength and modulus of samples at a strain rate of 1 mm/min. All samples were designed with dimensions of 127 mm × 12.7 mm × 3.175 mm. The support span used was 61 mm, which corresponds with a minimum span of 16 times the thickness of the samples as specified by the standard. Each data point is the average of at least 5 samples.

2.4.7. Thermal conductivity

Thermal conductivity was measured using the transient plane source method (TPS 2500S) with sensor 7577 (4.002 mm diameter). The samples tested had average dimensions of 60 mm × 30 mm × 2 mm and were tested under anisotropic conditions with 15 mW for 1 s. The anisotropic measurement provides the thermal conductivity in axial (through thickness) and radial directions. Each data point shown is an average of 5 anisotropic measurements.

3. Results & discussion

3.1. Optical microscopy of nanoparticle dispersion

Optical micrographs of the ABS nanocomposite films in Fig. 3a–e shows the macroscopic agglomeration state of CNT-CNC. It is noted that with increasing nanofiller concentration, the number visible micron-sized agglomerates also increase. The results at first seem to mirror findings by Wang et al., where they report an increase in the size and agglomerations (5–10 μm at 1–5% and 30–100 μm at 10%) in PLA/CNT nanocomposites with loadings up to 10% [53]. Upon inspection of higher magnification micrographs as shown in Fig. 4, the agglomerates are not all completely opaque but are partially translucent due to the dispersion of CNTs within CNCs. This indicates that while large agglomerations of CNTs do exist within the nanocomposite, the majority exists within sub-agglomerates in CNCs. In essence, solid Pickering emulsions of CNT-CNC are observed. This phenomenon has been studied by Yu et al., where PLA/CNC/CNT composites were fabricated by first creating PLA/CNC/CNT microparticles by Pickering emulsions [44].

With PLA, agglomeration occurs due to the phase mismatch between hydrophobic CNT and hydrophilic PLA/CNC. In comparison to PLA, ABS has a lower ability to disperse CNCs. While PLA is hydrophilic due to the high quantities of hydroxyl groups, ABS has limited hydrophilicity from the permanent dipoles in the acrylonitrile monomers. Having styrene in the terpolymer can further assist in the direct dispersion of CNT through π-π interactions, which has been demonstrated in shear exfoliated PEEK-graphene nanocomposites [54]. From previous works on these nanomaterials, it has been noted that the hydrodynamic diameter of CNT-CNC in DI water is 140 nm, indicating that the agglomerates should theoretically have a smaller true diameter once dried and dispersed. However, it must be noted that agglomeration occurs between neighboring CNT-CNC particles during the drying process when coating the ABS pellets. Thus, agglomerate size and quantity using our methods is dependent on two key factors: first the ability for CNC to individually wrap CNTs during the sonication process, and second the ability for extrusion to shear exfoliate large CNT-CNC clusters.

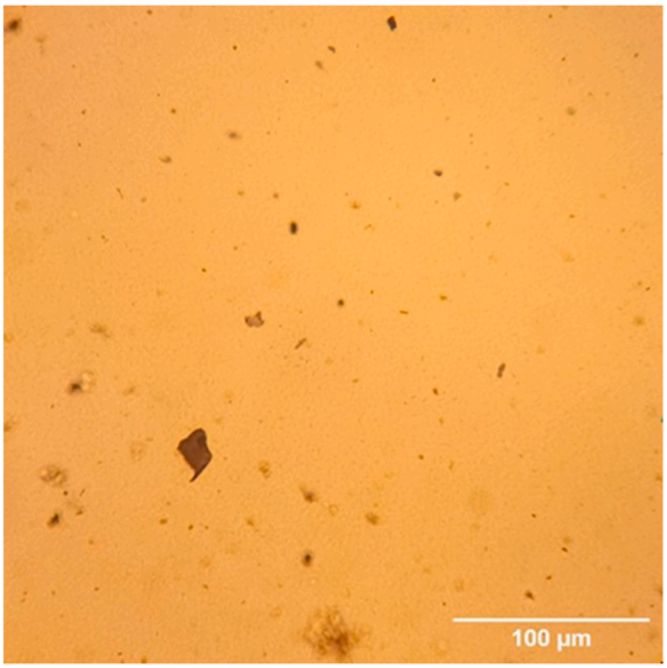

Fig. 4. Optical micrographs at 40× magnification of ABS - 2% CNT-CNC nanocomposite.

3.2. Thermal stability & CNT-CNC content

TGA scans reveal that the effect of the nanofillers does not significantly affect the thermal stability of the nanocomposite, due to both the low concentrations of nanoparticles and the atmospheric air environment that was used for testing. Despite this, the scans help uncover some of the mechanisms by which thermal stability is impacted through the inclusion of CNT-CNC. In Fig. 5a, ABS shows two decomposition steps, the primary at ~410 °C and the secondary at ~560 °C. According to literature, the primary step can be attributed to the general thermo-oxidization of the terpolymer beginning with polybutadiene and the formation of volatile aromatics [53,54]. The secondary step is the scission of C–C bonds of residual graphitic char formed from styrene-acrylonitrile, as polyacrylonitrile is known to be a precursor to carbon fiber. This secondary step matches the onset degradation temperature of CNTs, thus the difference in char between ABS and its nanocomposite can be used to estimate the true concentration of the nanomaterials. Results of concentration characterization are summarized in Table 2. Although the difference to the theoretical are relatively low, error can be primarily attributed to residual char from CNC/ABS, and coating thickness variations adsorbed on the ABS pellets' surfaces.

Observing the derivative scan in Fig. 5b, the subtle effects of the addition of CNCs and CNTs are observed on the decomposition rate. After desorption of moisture in CNCs from heating up to 200 °C, it is shown from literature that cellulose decomposition begins after 240 °C through the removal of hydroxyl groups and subsequent increased conjugation of the char [55]. Since CNCs are fully embedded within the ABS without direct exposure to O_2, the degradation effect is tempered and only marginally reduces the onset degradation of ABS. The onset thermal degradation of PAN/CNC is insignificant at loadings below 20%, but significant at 40%, which is in accordance with other reports [56]. Regarding CNTs, previous works have shown no significant effect on the onset thermal degradation [9,39,57], or a marginal reduction in the onset decomposition rate [58]. According to Yang et al., it is hypothesized that CNTs can catalyze the initial decomposition step of ABS, but at higher temperatures the decomposition products of ABS are stabilized [59]. This shows to be in agreement with the results shown in Fig. 5b, as the decomposition rate between 425 °C and 475 °C is lowered with the addition of CNTs. The slight increase decomposition rate onwards looks to coincide with the last degradation step of cellulose. Here, cellulose is expected to continue to undergo chain scission and further aromatization [55,56].

3.3. Tensile properties

The effect of the addition of CNT-CNC in ABS on tensile properties are plotted in Fig. 6. In nearly all of the sample concentrations tested, an increase in tensile strength from the neat ABS samples is present, shown in Fig. 6b. Most notably, the angle ply road orientation exhibits an 81% increase in tensile strength in the 2 wt% concentration and 45% increase in the 1 wt% concentration. The nanocomposite concentrations that are less than 1 wt% do not show a significant increase, which indicates that

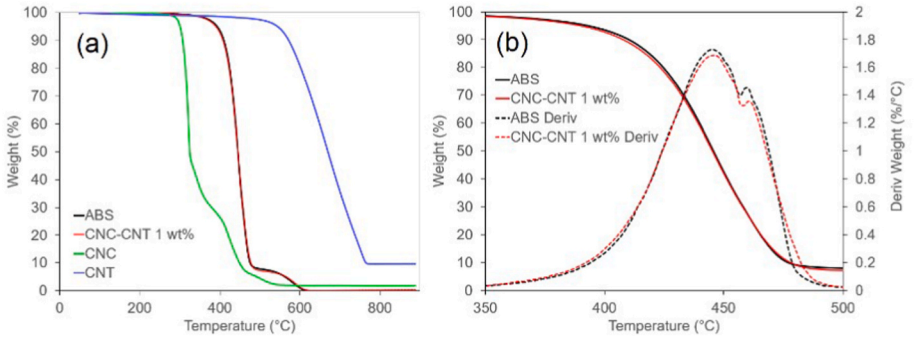

Fig. 5. (a) TGA curves of the ABS nanocomposite, nanofillers CNCs, and CNTs. (b) TGA and DTG curves of the ABS nanocomposite at the primary decomposition step.

Table 2
Experimentally derived CNT-CNT concentrations in nanocomposites.

Sample	Actual CNT-CNC Concentration
0.2 wt% CNT-CNC	0.21 wt% CNT-CNC
0.5 wt% CNT-CNC	0.68 wt% CNT-CNC
1 wt% CNT-CNC	1.12 wt% CNT-CNC
2 wt% CNT-CNC	2.16 wt% CNT-CNC

the optimum CNT-CNC levels are higher than at least 1 wt%. Though the angle ply samples offer the highest increase in tensile strength, the longitudinal and transverse samples show increase in the larger concentrations (1 and 2 wt%) of CNT-CNC. This tensile strength increase can be attributed to the reinforcement that the CNT-CNC offers to the ABS matrix, especially when larger numbers of these nanoparticles are present in the material, as the tensile strength of the CNTs is exponentially higher than ABS. The drastic increase in tensile strength in angle ply, relative to longitudinal and transverse specimens can be attributed to improvements in the shear strength. Finite element study by Gonabadi et al. on road orientation v. mechanical properties show that specimens of 45/45 exhibit higher shear strengths relative to longitudinal, but lower normal strengths [60]. While the effects of the CNT-CNC concentrations are being studied, it must be noted that the print orientation of the samples does have a large influence in the mechanical properties of the samples. While 0/90 orientations look to maximize the loading capabilities in the normal loading directions, angled road orientations allow filament alignment towards the principal directions of shear. This indicates that the angle in which these samples are printed must be optimized as well, which, in this case, would be in the angle ply direction that happens to be the default direction of the printer's slicing software. With the alternating angle of each layer, the tensile stress is transferred to the CNT-CNC reinforcements in even and opposite directions that create higher ultimate strengths.

The modulus of elasticity, displayed in Fig. 6a, shows a similar trend to that of the ultimate tensile strength discussed above. In the angle ply orientation, the modulus of elasticity increases as the concentration of the CNT-CNC does, further expressing the trend seen in the strength property. The CNT-CNC itself does add stiffness, and with the proper orientation can improve the elastic modulus nearly 1 GPa (a 95% increase) over the neat ABS concentration, seen in the 1 wt% CNT-CNC specimen. Additionally in the angle ply oriented samples, the elastic modulus of the 0.5 and 2 wt% displayed an increase in value by 72% and 41%, respectively. As before, the longitudinal and transverse directions do not experience rising trends and do not exhibit an elastic modulus

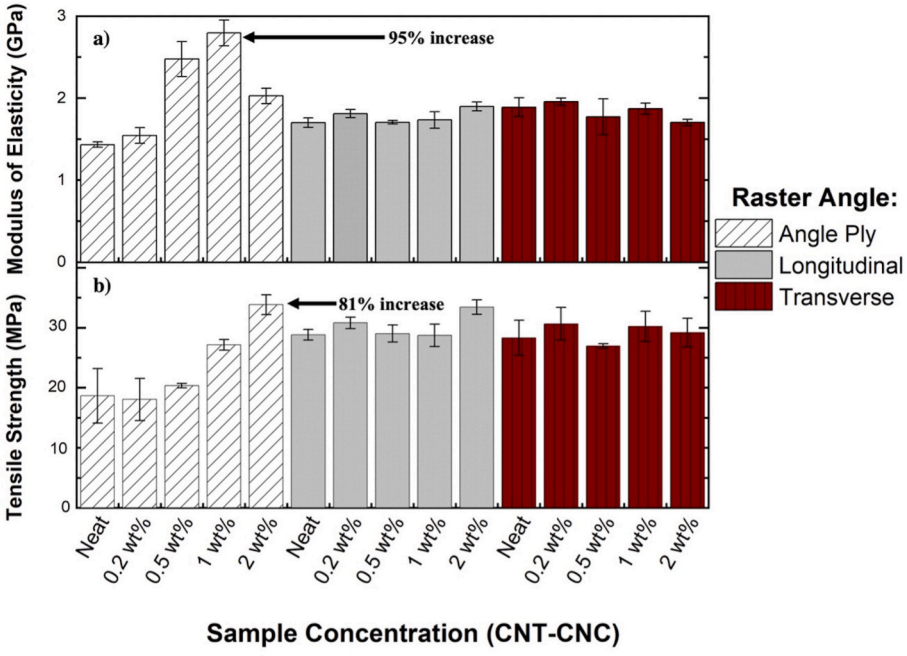

Fig. 6. a) Modulus of elasticity and b) tensile strength of nanocomposite samples printed in angle ply, longitudinal, and transverse print orientations. Increasing trends in these properties are observed in the angle ply print orientation, where the other two directions show limited change in properties.

that is highly improved from the neat ABS counterpart. Again, the larger concentrations of nanoparticles in these orientations did have a slight increase in the modulus, though the road orientation plays an important role in an increasing trend as well.

In evaluating the stress-strain diagrams, Fig. 7, that accompany the champion 2 wt% CNT-CNC samples, tensile properties increase with the addition of nanoparticle reinforcements. The neat ABS in all three road angles exhibits lower ultimate tensile strength than the 2 wt% CNT-CNC samples, though the angle ply orientation notably had the lowest strength. As shown in Fig. 6b, the tensile strength of 0.2, 0.5, and 1 wt% samples printed in the angle ply orientation exhibited the lowest ultimate strengths. However, the print orientation shows little effect with 2 wt% CNT-CNC additions, where the stress strain curves of ABS nanocomposites are nearly identical in modulus of elasticity and ultimate strength. This suggests that the larger concentrations of nanomaterials have a greater influence on these properties than the road angle, and it is hypothesized that this trend would follow with larger amounts of CNT-CNC, until the saturation point is met. In all of the 2 wt% CNT-CNC samples, there is little change in the average strain at break values, which suggests that the nanoparticles do not cause premature fracture due to embrittlement. Additionally, with the increase in CNT-CNC in the nanocomposite parts, there is a subsequent increase in the toughness of the material, when compared to neat, which stems from a combination of the increased tensile strength, elastic modulus, and strain at break.

3.4. Interlaminar shear strength

Fig. 8 plots the interlaminar shear strength (ILSS), which was used to measure the effect of CNT-CNC content on the interlaminar adhesion of printed parts. The angle ply orientation shows an increasing trend as the CNT-CNC content increases, especially in the 0.2 and 0.5 wt% with 101% and 92% increases respectively, indicating that the interlaminar adhesion is strengthened by the pinning effect of CNT-CNC. When evaluating the 1 wt% concentration in the angle ply orientation, the improvement decreases, which suggests that the ideal nanoparticle concentration is within the 0.2–0.5 wt% range due to potential agglomerations that may occur at the higher concentrations of CNT-CNC. In the transverse samples, an increasing trend is exhibited as well, with the 1 wt% CNT-CNC samples improving the ILSS property by 14%, which is very similar to the increase seen in the angle ply specimens. The 0.2 and 0.5 wt% concentrations increase in a positive linear trend from

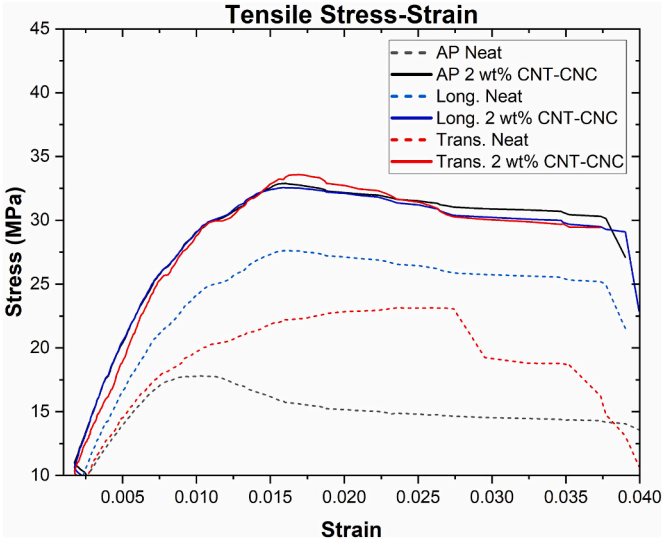

Fig. 7. Stress-strain diagrams for nanocomposite concentrations using angle ply (AP), longitudinal (Long.), and transverse (Trans.) road angles, confirming the increase in tensile strength in the angle ply road angle.

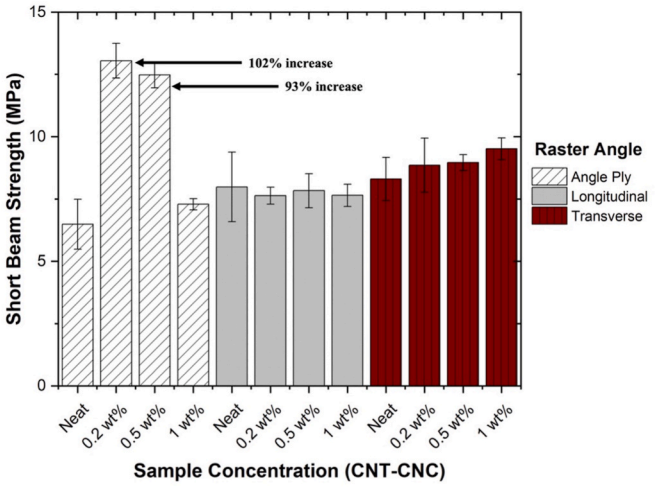

Fig. 8. Short beam shear strength of nanocomposite samples printed in angle ply (A.P.), longitudinal (Long.), and transverse (Trans.) print orientations. Increase in this property is observed in the angle ply orientation, where the other two directions show limited change in properties.

the neat ABS samples, but at a subtle rate, implying that the ideal concentration for this print orientation is at least 1 wt%. However, in the samples which were printed with longitudinal roads, there is neither an enhancement nor decrease in the interlaminar adhesion. This indicates that the alternating roads which compose the angle ply-oriented samples are beneficial to the interlaminar adhesion of nanocomposite printed parts due its ability to transfer stress more efficiently than its longitudinal or transverse counterparts, as referenced previously. These results suggest that the road angle is as influential on the ILSS as the concentration of CNT-CNC itself and optimizing these two parameters simultaneously is imperative to maximize the interlaminar adhesion of printed parts.

3.5. Flexural strength

In contrast to the interlaminar shear strength, the flexural strength of the nanocomposite parts evaluates the tensile and compressive stresses that are administered in a 3-point bending mode, shown in Fig. 9. In this mode, the addition of CNT-CNC does not have a significant effect on the flexural strength of the parts, regardless of the direction that they were printed in. However, in the samples printed with the longitudinal road angle, the flexural strength for all 5 concentrations tested is higher than angle ply or transverse in this mode. This implies that the uninterrupted roads in the longitudinal orientation are best suited for the flexural load that is applied, which eliminates any discontinuities that would cause a failure prematurely. However, the concentrations of CNT-CNC do not have a significant bearing on the flexural properties directly. It is important to note that the simultaneous tensile and compressive stresses imparted on the nanocomposite samples in this test do not cause a decrease in properties either due to the stiffening nature that the CNT has as a reinforcing material. This leads to the conclusion that the CNT-CNC additions as well as the road angles do not detract from the material's ability to be utilized in a bending application.

3.6. Thermal conductivity

The axial (out-of-plane) and radial (in-plane) thermal conductivity values are evaluated for each nanocomposite sample as well as the three printing orientations to determine if the CNT-CNC or print direction have any bearing on the resulting thermal conductivity. Fig. 10a illustrates the directions that were measured for the anisotropic samples.

The thermal conductivity measurements are shown in Fig. 10b-c.

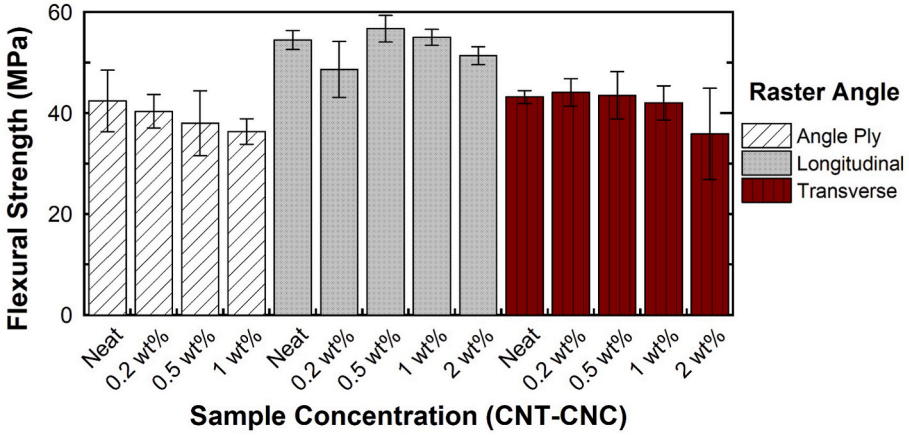

Fig. 9. Flexural strength of nanocomposite samples printed in angle ply, longitudinal, and transverse print orientations. The longitudinal samples showed the highest flexural strength; however, the property remains largely unchanged in all the print orientations and sample concentrations.

Beginning with the angle ply orientation, the axial thermal conductivity experiences a decreasing trend with the increased CNT-CNC concentrations, Fig. 10b. When observing the conductivity of these same samples in the radial direction, Fig. 10c, the "champion" values directly juxtapose those recorded in the axial direction. The contrasting values between these two measured directions imply that the orientation of the CNT-CNC themselves within the ABS matrix are the driving force behind increasing the thermal conductivity. Increased conductivity in the radial direction primarily occurs through flow-induced shear alignment of the nanofillers in the filament line direction during extrusion [61,62]. The effect of shear alignment depends on whether the particle has a rod-like shape for shear to induce rotation. From the optical microscopy results in Fig. 4, it is seen that macroscopic CNT-CNC agglomerates do not strictly maintain a rod or sheet-like shape from the bundled CNTs. CNTs may be loosely entangled to form spherical shapes but are then further encapsulated by CNCs creating larger round particulates. Shear alignment may be occurring for well-dispersed CNTs that are not visible with optical microscopy.

Review by Han and Fina summarizes that carbon nanotubes will typically improve thermal conductivity, but have severe limitations due to thermal resistance at the interface, dispersion, and contact resistance between nanotubes [63]. This explains why the radial direction consistently has a higher thermal conductivity but exhibits randomized improvements. The specimens tested in this study do not show a typical increase in thermal conductivity with concentration as expected by following the rule of mixtures at higher concentrations [64]. The marked increase in specific concentrations is indicative that the percolation threshold varies based on the concentration applied. Both dispersion and the inclusion of CNCs are the primary factors to consider. Single screw extrusion has limitations on uniform dispersion versus twin-screw extrusion, as twin-screw extruders create larger but more highly branched aggregates [65]. More importantly, CNCs theoretically have a low bulk thermal conductivity from 0.25 to 0.53 W/m-K based on shear alignment of bulk CNC [66]. Additionally, encapsulation of CNTs with CNCs will significantly increase the interface resistance between ABS and CNCs. Considering the lack of control of agglomeration during the coating process of the pellets, it is likely that CNTs have inconsistent CNC encapsulation thicknesses, resulting in large variations in the interface resistance between particles.

Because ABS is an amorphous polymer, there is no additional alignment effect induced from the crystallization of the resin. It can therefore be concluded that the thermal conductivity is highly dependent on the orientation of the CNT-CNC, dispersion, and the encapsulation of CNTs with CNCs. The heat will therefore be conducted in the direction where it can dissipate the fastest, which may not follow a particular trend at these low concentrations due to the increased interface resistance from CNCs.

Comparing the differences between road orientations, in the angle ply samples there is a decreasing trend in the thermal conductivity in the axial direction, while exhibiting increases in each nanocomposite concentration in the radial concentration, supporting the juxtaposition of the two measured directions. The champion sample for the radial direction was the 1 wt% CNT-CNC, with an 807% increase from the neat ABS sample, Fig. 10c. However, at the higher 2 wt% concentration, the radial conductivity decreases again, suggesting that an oversaturation of the nanomaterial occurs over 1 wt%. A similar trend is seen in the longitudinally printed samples, where the 0.5 wt% CNT-CNC concentration experienced a diminished axial thermal conductivity (Fig. 10b) while simultaneously increasing 269% over its neat counterpart in the radial direction (Fig. 10c). Once again, there is a random pattern observed within each measured direction, but a correlation within each sample concentration having an improved radial or axial value, but not both.

The nanocomposite samples printed using transverse road angles exhibited a more conventional trend pattern than the angle ply and longitudinal counterparts, specifically in the axial direction (Fig. 10b). The 0.2 wt% CNT-CNC sample exhibited the highest thermal conductivity in the out-of-plane direction, with a 96% increase over the neat ABS. Increasing the nanoparticle concentration past 0.2 wt% decreased the thermal conductivity, indicating that the addition of CNT-CNC above this point creates an oversaturation in the material for this property. However, upon examination of the thermal conductivity in the radial direction of these samples (Fig. 10c), there is a different trend. The 0.2 wt%, 0.5 wt%, and 1 wt% concentrations all have a similar increase in radial conductivity with a larger increase at the 2 wt% concentration. Once again, there exists a relationship between the radial and thermal conductivity values for each sample, where the thermal conductivity is only increased significantly in one direction, but not both.

3.7. Fracture surface morphology

3.7.1. Tensile specimen

The fracture surface of the post-mortem tensile angle ply specimens, normal to the applied force, is examined to further evaluate the failure mechanisms. The fracture surfaces of the angle ply orientation reveal that the addition of the CNT-CNC nanoparticles did alter the fracture compared to the neat ABS control sample. Fig. 11b–c, shows that the fracture surface exhibits single roads in all three of the nanocomposite concentrations, while this feature is not present on the neat ABS sample, Fig. 11a. As the CNT-CNC concentration increases, the individual roads become more defined on the surface, which directly correlates with the increased tensile strength properties previously discussed in Fig. 6. The

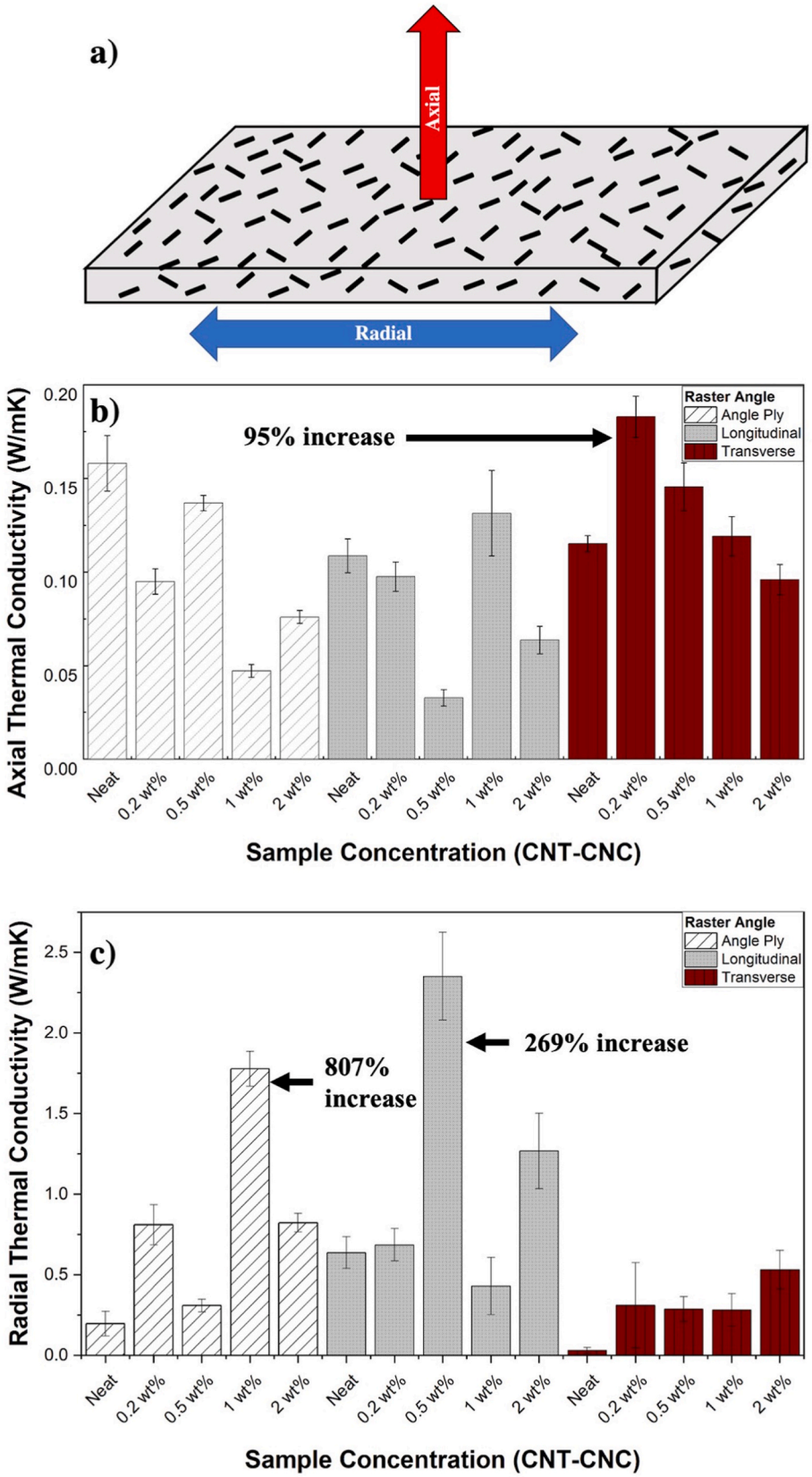

Fig. 10. a) Anisotropic thermal conductivity measurements recorded in the axial (out-of-plane) and radial (in-plane) directions for each nanocomposite sample. Thermal conductivity of nanocomposite samples measured in b) axial (out-of-plane) and c) radial (in-plane) directions of samples printed in angle ply, longitudinal, and transverse print orientations. In the radial direction, the 0.2 wt% CNT-CNC sample printed in the transverse direction exhibited a 95% increase in conductivity from neat. In the radial direction, the 1 wt% CNT-CNC angle ply sample saw an 807% increase and the 0.5 wt% CNT-CNC longitudinal sample measured a 269% increase in conductivity from neat samples. Improvements in conductivity in each road direction are observed in either the radial or axial direction, but not both. The transverse direction experiences the largest and most consistent increasing trend of all the orientations.

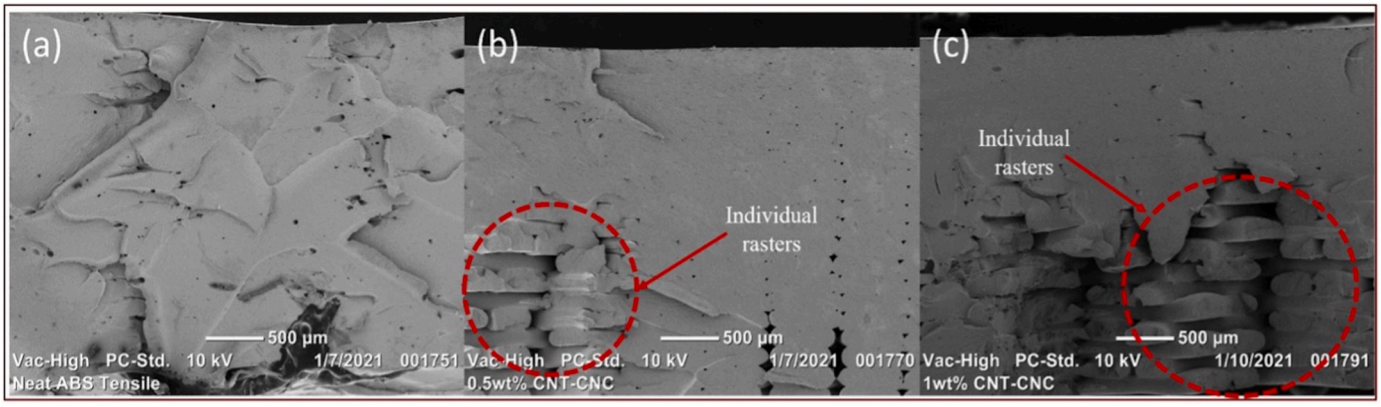

Fig. 11. SEM images of fracture surfaces on tensile samples printed in angle ply orientation including concentrations of (a) neat ABS, (b) 0.5 wt% CNT-CNC, and (c) 1 wt% CNT-CNC.

difference in fracture behavior corresponds with the ability of the ABS matrix to transfer the applied stress to the reinforcement, therefore increasing the tensile strength and additionally relying on the individual roads themselves to withstand a larger applied force. Furthermore, the fracture surface roughness seen in the 0.5 wt% and 1 wt% concentrations (Fig. 11b–c, respectively), exhibit failure mechanisms that are unique from the neat ABS sample. This is due to the nanocomposite counterparts' ability to absorb a greater quantity of energy prior to fracture than the control sample, which behaves more as a bulk material than one that had been processed with AM. Therefore, the individual roads become more pronounced because of a higher energy that is absorbed.

3.7.2. Interlayer shear strength specimen

The SEM images captured of the short beam test angle ply samples were taken after fracture, shown in Fig. 12. In these specimens, the crack propagation patterns are notably different in the nanocomposites when compared to the neat ABS. With the neat ABS sample shown in Fig. 12a, the crack is straight with no reinforcing nanomaterials to alter the crack's path of travel as the material fails and fractures. In the 0.5 wt% and 1 wt% concentrations, Fig. 12b–c respectively, the crack propagation exhibits a non-linear, zig-zag behavior, indicating that the crack is arrested when reaches the stiff nanomaterials and changes its path, suggesting that higher energy will be consumes during fracture. These results correlate with the higher ILSS value for 0.5 wt% in Fig. 8. Additionally, when evaluating the crack propagation behavior of these samples, it is notable that there is no visible delamination of adjacent layers, including the neat samples, which is attributed to the better adhesion between neighboring layers.

3.7.3. Flexural specimen

The crack propagation behavior of flexural angle ply samples examined using SEM are shown below in Fig. 13, exhibit a similar trend in regard to the nature of the crack spreading down the side of the sample. In these samples, the non-linear crack propagation is most notable in the 1 wt% CNT-CNC sample shown in image (Fig. 13c). In the case of flexural properties as discussed previously, they remain statically unchanged from the neat ABS, meaning that the unique crack propagation seen in the 1 wt% CNT-CNC specimen does not correspond to the flexural properties directly. Ultimately, the SEM images reveal the continued absence of delamination when utilizing the angle ply road orientation, and that the CNT-CNC additions harness the ability to redirect the applied stress from the ABS matrix itself.

4. Conclusion

This work introduces a novel scalable processing method that harnesses a binary, hybrid nanoparticle system to improve mechanical performance and functionality to 3D printed parts. The use of hydrophilic CNCs to bond to hydrophobic pristine CNTs and disperse them in an aqueous medium presents a new processing approach in which assisting reinforcing nanomaterials are used to coat ABS feedstock. This method harnesses a binary, hybrid nanoparticle system to impart multifunctionality in parts created through FFF printing, through a synergistic relationship between the CNTs and CNCs used. Therefore, this work presents an attractive and cost-effective option for high quality AM parts that could be used in the place of metallic parts, offering a lightweighting alternative to aluminum and steel components. The manufacturing technique and hybrid nanocomposite filament created aim to improve the quality, accessibility, and scalability of high

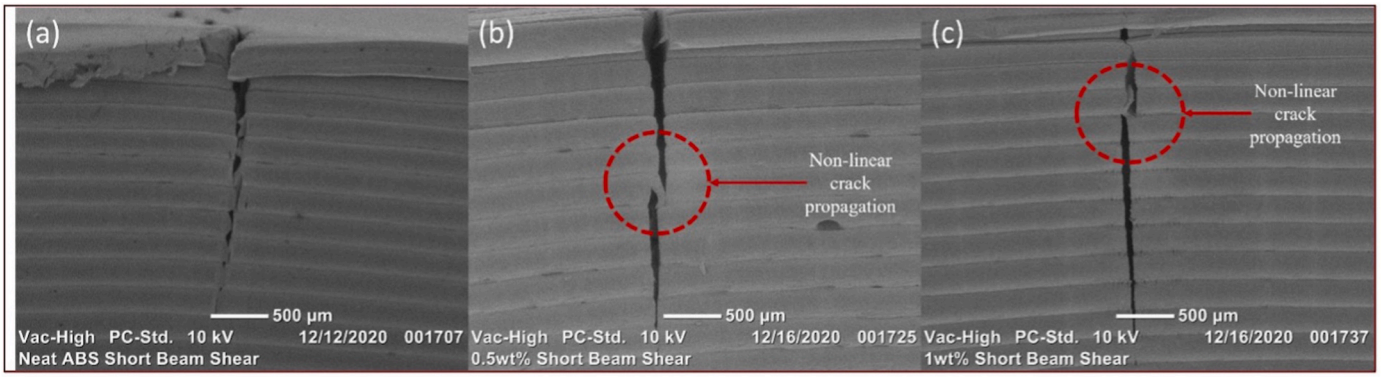

Fig. 12. SEM images of crack propagation on the side of interlaminar shear strength specimen printed in angle ply orientation including concentrations of (a) neat ABS, (b) 0.5 wt% CNT-CNC, and (c) 1 wt% CNT-CNC.

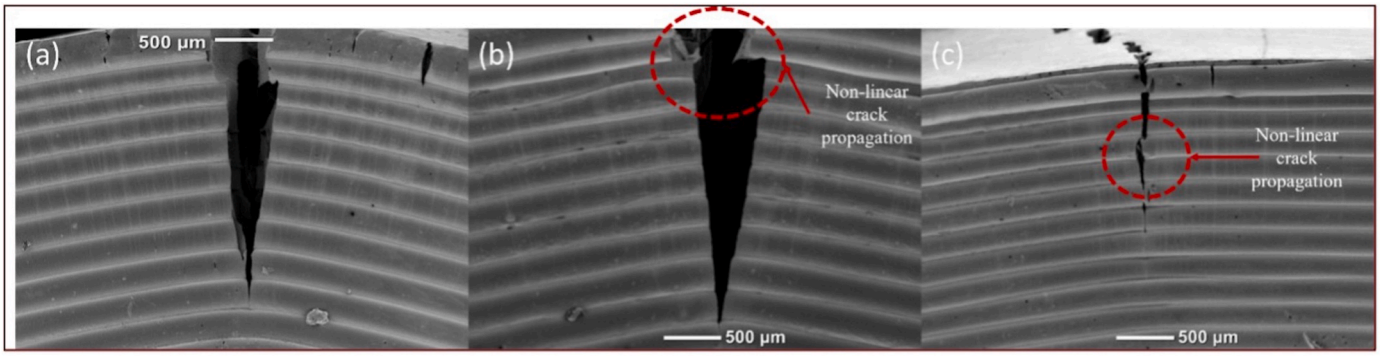

Fig. 13. SEM images of crack propagation on the side of flexural specimen printed in angle ply orientation including (a) neat ABS, (b) 0.5 wt% CNT-CNC and (c) 1 wt % CNT-CNC.

strength, functional 3D printed parts for use in automotive and aerospace applications.

The effects of the hybrid CNT-CNC nanoparticle system and road orientations were studied in unison, to determine the codependence of materials, processing including road orientations and resulting properties. The improvement of tensile, flexural and interlaminar shear strength properties were more pronounced with the increase in concentration of CNT-CNC in angle ply road (the default of 3D orienting in most of FFF printers) compared to those of transverse and longitudinal samples. When considering thermal conductivity, it was discovered that there was a relationship between the radial and axial thermal conductivity, where there is only an increase in one of the two directions, but not both, which signifies the role of alignment of the CNT-CNC within the amorphous ABS matrix. The combination of mechanical and functional properties portrays that the print road angles, and the nanomaterials concentrations affect the performance cooperatively, reflecting that optimizing these properties for the feedstock are required for maximized functionality and structural performance of the end use.

Author statement

Mia Carrola: Conceptualization, Methodology, Formal Analysis, Investigation, Writing - Original Draft, Visualization.

Emile Motta De Castro: Formal Analysis, Investigation.

Ali Tabei: Formal Analysis, Investigation.

Amir Asadi: Conceptualization, Writing - Review & Editing, Supervision, Project Administration.

Declaration of competing interest

The authors declare that they have no known competing financial interests or personal relationships that could have appeared to influence the work reported in this paper.

Data availability

Data will be made available on request.

Acknowledgements

This material is based upon work supported by the National Science Foundation under Grant# 1930277 and Grant #: EEC 1757882, REU Site in Cybermanufacturing. Any opinions, findings, conclusions, or recommendations presented are those of the authors and do not necessarily reflect the view of the National Science Foundation.

Appendix A. Supplementary data

Supplementary data to this article can be found online at https://doi.org/10.1016/j.polymer.2023.125980.

References

[1] M. Mohammed, et al., Customised design and development of patient specific 3D printed whole mandible implant, Proc. 27th Ann. Int. Solid Freeform Fabr. Sympos. (2016) 1708–1717.
[2] P. Wu, J. Wang, X. Wang, A critical review of the use of 3-D printing in the construction industry, Autom. ConStruct. 68 (2016) 21–31.
[3] S.H. Huang, et al., Additive manufacturing and its societal impact: a literature review, Int. J. Adv. Des. Manuf. Technol. 67 (5) (2013) 1191–1203.
[4] M. Dawoud, I. Taha, S.J. Ebeid, Mechanical behaviour of ABS: an experimental study using FDM and injection moulding techniques, J. Manuf. Process. 21 (2016) 39–45.
[5] J. Wang, et al., A novel approach to improve mechanical properties of parts fabricated by fused deposition modeling, Mater. Des. 105 (2016) 152–159.
[6] K. Günaydın, H.S. Türkmen, Common FDM 3D printing defects, in: International Congress on 3D Printing (Additive Manufacturing) Technologies and Digital Industry, 2018.
[7] T.D. Ngo, et al., Additive manufacturing (3D printing): a review of materials, methods, applications and challenges, Compos. B Eng. 143 (2018) 172–196.
[8] X. Wang, et al., 3D printing of polymer matrix composites: a review and prospective, Compos. B Eng. 110 (2017) 442–458.
[9] S. Dul, L. Fambri, A. Pegoretti, Filaments production and fused deposition modelling of ABS/carbon nanotubes composites, Nanomaterials 8 (1) (2018) 49.
[10] H.K. Sezer, O. Eren, FDM 3D printing of MWCNT re-inforced ABS nano-composite parts with enhanced mechanical and electrical properties, J. Manuf. Process. 37 (2019) 339–347.
[11] S. Singh, S. Ramakrishna, R. Singh, Material issues in additive manufacturing: a review, J. Manuf. Process. 25 (2017) 185–200.
[12] D. Popescu, et al., FDM process parameters influence over the mechanical properties of polymer specimens: a review, Polym. Test. 69 (2018) 157–166.
[13] A. Dorigato, et al., Electrically conductive nanocomposites for fused deposition modelling, Synth. Met. 226 (2017) 7–14.
[14] M. Petousis, et al., Multifunctional material extrusion 3D-printed antibacterial polylactic acid (PLA) with binary inclusions: the effect of cuprous oxide and cellulose nanofibers, Fibers 10 (6) (2022) 52.
[15] K. Gnanasekaran, et al., 3D printing of CNT-and graphene-based conductive polymer nanocomposites by fused deposition modeling, Appl. Mater. Today 9 (2017) 21–28.
[16] M.F. Arif, et al., Multifunctional performance of carbon nanotubes and graphene nanoplatelets reinforced PEEK composites enabled via FFF additive manufacturing, Compos. B Eng. 184 (2020), 107625.
[17] G. Spinelli, et al., Morphological, Rheological and electromagnetic Properties of nanocarbon/poly(lactic) Acid for 3D printing: solution Blending vs. melt mixing, Materials 11 (11) (2018) 2256.
[18] A. Mora, P. Verma, S. Kumar, Electrical conductivity of CNT/polymer composites: 3D printing, measurements and modeling, Compos. B Eng. 183 (2020), 107600.
[19] D. Rigotti, L. Fambri, A. Pegoretti, Polyvinyl alcohol reinforced with carbon nanotubes for fused deposition modeling, J. Reinforc. Plast. Compos. 37 (10) (2018) 716–727.
[20] E.R. Cholleti, I. Gibson, ABS nano composite materials in additive manufacturing, in: IOP Conference Series: Materials Science and Engineering, IOP Publishing, 2018.
[21] D. Xiang, et al., Enhanced performance of 3D printed highly elastic strain sensors of carbon nanotube/thermoplastic polyurethane nanocomposites via non-covalent interactions, Compos. B Eng. 176 (2019), 107250.
[22] K. Kim, et al., 3D printing of multiaxial force sensors using carbon nanotube (CNT)/thermoplastic polyurethane (TPU) filaments, Sensor Actuator Phys. 263 (2017) 493–500.
[23] T.-H. Le, et al., Microstructure evaluation and thermal–mechanical properties of abs matrix composite filament reinforced with multi-walled carbon nanotubes by a single screw extruder for fdm 3d printing, Appl. Sci. 11 (19) (2021) 8798.

[24] N. Vidakis, et al., Mechanical and electrical properties investigation of 3D-printed acrylonitrile–butadiene–styrene graphene and carbon nanocomposites, J. Mater. Eng. Perform. 29 (3) (2020) 1909–1918.
[25] J. Horst, et al., Fabrication of conductive filaments for 3D-printing: polymer nanocomposites. Biointerface Research, Appl. Chem. 10 (6) (2020) 6577–6586.
[26] L. Yang, et al., Effects of carbon nanotube on the thermal, mechanical, and electrical properties of PLA/CNT printed parts in the FDM process, Synth. Met. 253 (2019) 122–130.
[27] N. Vidakis, et al., Additive manufacturing of multifunctional polylactic acid (PLA)—multiwalled carbon nanotubes (MWCNTs) nanocomposites, Nanocomposites 7 (1) (2021) 184–199.
[28] R.H. Sanatgar, C. Campagne, V. Nierstrasz, Investigation of the adhesion properties of direct 3D printing of polymers and nanocomposites on textiles: effect of FDM printing process parameters, Appl. Surf. Sci. 403 (2017) 551–563.
[29] V. Tambrallimath, et al., Mechanical characterization of PC-ABS reinforced with CNT nanocomposites developed by fused deposition modelling, in: Journal of Physics: Conference Series, IOP Publishing, 2020.
[30] E. Ivanov, et al., PLA/Graphene/MWCNT composites with improved electrical and thermal properties suitable for FDM 3D printing applications, Appl. Sci. 9 (6) (2019) 1209.
[31] M. Mohammadi, et al., Synthesis and crystallization of lead–zirconium–titanate (PZT) nanotubes at the low temperature using carbon nanotubes (CNTs) as sacrificial templates, Adv. Powder Technol. 23 (5) (2012) 647–654.
[32] K. Balasubramanian, M. Burghard, Chemically functionalized carbon nanotubes, Small 1 (2) (2005) 180–192.
[33] Y.-P. Sun, et al., Functionalized carbon Nanotubes: properties and applications, Acc. Chem. Res. 35 (12) (2002) 1096–1104.
[34] M. Garg, S. Sharma, R. Mehta, Pristine and amino functionalized carbon nanotubes reinforced glass fiber epoxy composites, Compos. Appl. Sci. Manuf. 76 (2015) 92–101.
[35] D. Trache, et al., Recent progress in cellulose nanocrystals: sources and production, Nanoscale 9 (5) (2017) 1763–1786.
[36] J. George, S. Sabapathi, Cellulose nanocrystals: synthesis, functional properties, and applications, Nanotechnol. Sci. Appl. 8 (2015) 45.
[37] Y. Habibi, L.A. Lucia, O.J. Rojas, Cellulose nanocrystals: chemistry, self-assembly, and applications, Chem. Rev. 110 (6) (2010) 3479–3500.
[38] P. Lu, Y.-L. Hsieh, Preparation and properties of cellulose nanocrystals: rods, spheres, and network, Carbohydrate Polym. 82 (2) (2010) 329–336.
[39] H. Chang, et al., Carbon fibers from polyacrylonitrile/cellulose nanocrystal nanocomposite fibers, Carbon 145 (2019) 764–771.
[40] J. Choi, et al., High performance carbon fiber structural batteries using cellulose nanocrystal reinforced polymer electrolyte, ACS Appl. Mater. Interfaces 14 (40) (2022) 45320–45332.
[41] S. Shariatnia, et al., Atomization of cellulose nanocrystals aqueous suspensions in fused deposition modeling: a scalable technique to improve the strength of 3D printed polymers, Compos. B Eng. 177 (2019), 107291.
[42] C. Olivier, et al., Cellulose nanocrystal-assisted Dispersion of luminescent single-walled carbon Nanotubes for layer-by-layer assembled hybrid thin films, Langmuir 28 (34) (2012) 12463–12471.
[43] J.-B. Mougel, et al., Highly efficient and predictable noncovalent dispersion of single-walled and multi-walled carbon nanotubes by cellulose nanocrystals, J. Phys. Chem. C 120 (39) (2016) 22694–22701.
[44] B. Yu, et al., Fabrication of PLA/CNC/CNT conductive composites for high electromagnetic interference shielding based on Pickering emulsions method, Compos. Appl. Sci. Manuf. 125 (2019), 105558.
[45] M.D.R. Batista, L.T. Drzal, Carbon fiber/epoxy matrix composite interphases modified with cellulose nanocrystals, Compos. Sci. Technol. 164 (2018) 274–281.
[46] H. Bi, et al., Fabrication of cellulose nanocrystal reinforced thermoplastic polyurethane/polycaprolactone blends for three-dimension printing self-healing nanocomposites, Cellulose 27 (14) (2020) 8011–8026.
[47] Kusmono and P, P. Aji. Fabrication and tensile properties of ABS/cellulose nanocrystal nanocomposite filaments for 3D printing, in: AIP Conference Proceedings, AIP Publishing LLC, 2021.
[48] X. Wu, et al., Melt-processed poly (L-lactic acid)/cellulose nanocrystals biocomposites for 3D printing: Improved melt processibility and inter-fuse adhesion, Compos. Sci. Technol. 218 (2022), 109135.
[49] Y. Liu, et al., Aqueous dispersion of carbon fibers and expanded graphite stabilized from the addition of cellulose nanocrystals to produce highly conductive cellulose composites, ACS Sustain. Chem. Eng. 6 (3) (2018) 3291–3298.
[50] O. Kaynan, L.M. Pérez, A. Asadi, Cellulose nanocrystal-enabled Tailoring of the Interface in carbon nanotube-and graphene nanoplatelet-carbon fiber polymer composites: Implications for structural applications, ACS Appl. Nano Mater. 5 (1) (2022) 1284–1295.
[51] S. Shariatnia, et al., Hybrid cellulose nanocrystal-bonded carbon nanotubes/carbon fiber polymer Composites for structural applications, ACS Appl. Nano Mater. 3 (6) (2020) 5421–5436.
[52] M. Aramfard, et al., Aqueous dispersion of carbon nanomaterials with cellulose nanocrystals: an investigation of molecular interactions, Small 18 (37) (2022), 2202216.
[53] L. Wang, et al., The relationship between microstructure and mechanical properties of carbon nanotubes/polylactic acid nanocomposites prepared by twin-screw extrusion, Compos. Appl. Sci. Manuf. 89 (2016) 18–25.
[54] J.K. Lynch-Branzoi, et al., Shear exfoliation of graphite into graphene nanoflakes directly within polyetheretherketone and a spectroscopic study of this high modulus, lightweight nanocomposite, Compos. B Eng. 188 (2020), 107842.
[55] M. Suzuki, C.A. Wilkie, The thermal degradation of acrylonitrile-butadiene-styrene terpolymei as studied by TGA/FTIR, Polym. Degrad. Stabil. 47 (2) (1995) 217–221.
[56] Thermal Decomposition Measurement of ABS Resin I, in Thermal Decomposition Measurement of ABS Resin I, 1995, p. 6.
[57] M.M. Tang, R. Bacon, Carbonization of cellulose fibers—I, Low temp. pyrolysis. Carbon 2 (3) (1964) 211–220.
[58] M.H. Al-Saleh, B.A. Al-Saidi, R.M. Al-Zoubi, Experimental and theoretical analysis of the mechanical and thermal properties of carbon nanotube/acrylonitrile–styrene–butadiene nanocomposites, Polymer 89 (2016) 12–17.
[59] S. Yang, et al., Thermal analysis of an acrylonitrile–butadiene–styrene/SWNT composite, Polym. Degrad. Stabil. 83 (3) (2004) 383–388.
[60] H. Gonabadi, et al., Investigation of the effect of raster angle, build orientation, and infill density on the elastic response of 3D printed parts using finite element microstructural modeling and homogenization techniques, Int. J. Adv. Manuf. Technol. (2022) 1–26.
[61] A.B. Sulong, J. Park, Alignment of multi-walled carbon nanotubes in a polyethylene matrix by extrusion shear flow: mechanical properties enhancement, J. Compos. Mater. 45 (8) (2011) 931–941.
[62] D.E. Yunus, et al., Shear induced alignment of short nanofibers in 3D printed polymer composites, Nanotechnology 27 (49) (2016), 495302.
[63] Z. Han, A. Fina, Thermal conductivity of carbon nanotubes and their polymer nanocomposites: a review, Prog. Polym. Sci. 36 (7) (2011) 914–944.
[64] D.-K. Lee, et al., Electrical and thermal properties of carbon nanotube polymer composites with various aspect ratios, Materials 15 (4) (2022) 1356.
[65] D. Veigel, et al., Comparison of nanocomposite dispersion and distribution for several melt mixers, Polymer 269 (2023), 125735.
[66] J.A. Diaz, et al., Thermal conductivity in nanostructured films: from single cellulose nanocrystals to bulk films, Biomacromolecules 15 (11) (2014) 4096–4101.